Experimental investigation on damage evolution in pre-corroded aluminum alloy 7075-T7651 under fatigue loading

Experimental investigation on damage evolution in pre-corroded aluminum alloy 7075-T7651 under fatigue loading

Haipeng Song[a,b,*], Changchun Liu[a], Hao Zhang[c], Xudong Yang[a], Yajun Chen[a], Sean B. Leen[d]

[a] *Sino-European Institute of Aviation Engineering, Civil Aviation University of China, China*

[b] *Jiangsu Province Key Laboratory of Aerospace Power System, China;*

[c] *College of Mechanical Engineering, Yangzhou University, China;*

[d] *Mechanical Engineering, College of Engineering and Informatics, NUI Galway, Ireland*

Abstract

This paper experimentally investigates the fatigue damage evolution in pre-corroded aluminum alloy (AA) 7075-T7651 via digital image correlation (DIC) and scanning electron microscopy (SEM). Three stages of fatigue damage evolution including damage accumulation, macro-crack initiation and propagation are identified and described via the combined analysis of damage severity curves and strain maps. The micro-cracking characteristics in the dominant fracture regions are examined by fractography analysis. The experimental results show that localized corrosion penetrated in the 'L-S' or 'L-T' surfaces promotes fatigue crack initiation, affecting crack nucleation location, cracking path, and is accompanied with quasi-cleavage fracture. Damage evolution and failure progression differed temporally and spatially between specimens for the same loading conditions, due to the stochastic diversity of localized corrosion. Multiple corrosion-induced cracks were observed to initiate and evolve under different loading conditions: three typical failure modes, viz. single crack fracture, multi-crack competition and multi-crack parallel growth, were observed to depend on loading condition and relative location of macro-crack initiation.

Keywords: Aluminum alloy; Pre-corrosion; Fatigue failure; Damage evolution; Digital image correlation

* Corresponding author.

E-mail address: hpsong@cauc.edu.cn (Haipeng Song).

1. Introduction

Aluminum alloy (AA) is an important aircraft structural materials, widely used in fuselage frames, bulkheads and wing skins, due to the advantages of high strength and low density[1]. However, Al alloys are susceptible to localized corrosion, such as pitting and exfoliation, in the aircraft service environment [2, 3]. It is well known that localized corrosion-enhanced fatigue cracking is a common and dangerous failure mode in aircraft aluminum structures [4]. Improved understanding of fatigue damage evolution and failure mechanisms in aluminum alloys with localized corrosion is therefore required to improve corrosion management of aircraft for improved flight safety and life extension.

Many researchers have experimentally investigated the fatigue performance of aluminum alloys with localized corrosion. Medved *et al.* conducted constant and variable amplitude fatigue tests on pre-corroded AA7475-T761 samples, showing that pre-existing localized corrosion led to a 40-50% reduction in fatigue life compared with un-corroded samples [5]. Genel *et al.* performed bending fatigue experiments on pre-corroded AA7075-T6, and found that the fatigue strength was reduced by about 60% due to the presence of corrosion pits [6]. Such significant fatigue properties degradation is mainly attributed to the crack initiation and propagation derived from localized corrosion. To provide more experimental details about this, fatigue crack initiation characteristics in pre-corroded aluminum alloys have been widely analyzed via post-failure fractographic observation. Walde *et al.* examined the fracture morphology of pre-corroded AA2024-T3 by scanning electron microscopy (SEM), indicating that corrosion pits caused multiple-site fatigue crack initiation [7]. Kim *et al.* found that fatigue cracks initiated from pits clustered as semi-elliptical surface micro-notches, rather than the deepest pits in AA7075-T6511 [8]. Using combined interrupted test and fractographic observation, Walde *et al.* demonstrated that crack initiation occurred essentially instantaneously on application of cyclic loading [9]. Jones *et al.* employed microscopy to study the corrosion pit-to-crack transition process of AA2024-T3, establishing that pit surface area, surrounding pit proximity and pit depth together determined when and where cracks form [10]. In addition to promoting fatigue crack nucleation, the effect of corrosion on fatigue crack propagation has also been experimentally investigated. Noelle *et al.* applied the crack surface marking method to determine the micro-crack growth rate of AA7050-T7451, and found that crack growth rate was independent of corrosion damage morphology [11]. Li *et al.* performed an SEM *in-situ* fatigue test to study the fatigue crack growth in pre-corroded AA6151-T6, showing that early stage of fatigue micro-crack propagation behavior can be described by K_I-K_{II} mixed mode analysis [12]. Joshi *et al.* monitored the propagation of short cracks on the surface of pre-corroded AA7075-T6 samples by optical microscopy, indicating that the short crack growth life in salt solution was about 18% lower than that of ambient air [13]. Obviously, fatigue loading conditions, e.g. maximum stress and stress ratio, affect crack initiation and propagation in pre-corroded aluminum alloy. In fatigue experiments on pre-corroded AA2024, Walde *et al.* showed a correlation between maximum stress and the number of pits converted into cracks [7]. Burns *et al.* used the crack marking bands method to show that cycle of fatigue crack formation gradually decreased as maximum stress increased in pre-corroded AA7075-T651 [14]. From fatigue tests on AA2024-T62 specimens immersed in 3.5% sodium chloride solution at different stress ratios, Liu *et al.* showed that the crack growth rate of pre-corroded specimens at a stress ratio of -1 was significantly greater than for un-corroded specimens; while corrosion did not increase the rate of crack growth for stress ratio of 0.06 [15].

Based on experimental observation and analysis, some modelling work has also been conducted to analyze the damage evolution and crack propagation in aluminum alloys with localized corrosion, mainly employing damage mechanics and fracture mechanics. For example, a continuum damage mechanics model has been used by Amiri *et al.* to study corrosion-fatigue crack initiation of AA2024-T3, assumed that only one pit grows to a critical depth and transitions to a fatigue crack, despite the occurrence of multiple corrosion pits [16]. Hu *et al.* presented a coupled elastic-plastic damage and pit evolution model to predict corrosion fatigue life of aluminum alloy [17]. McMurtrey *et al.* applied linear elastic fracture mechanics with an equivalent initial defect size to predict fatigue life of corroded AA7075-T6511 under variable amplitude loading, achieving agreement to within 15% compared with experimental results [18]. Similarly, Xiang *et al.* combined an asymptotic model-I stress intensity factor (SIF) solution with a corrosion pit growth function for fatigue life prediction of pre-corroded specimens [19], while Wang *et al.* presented a cumulative crack growth methodology, based on the Willenborg-Chang rule, to evaluate residual life of aluminum alloy under corrosion-fatigue conditions [20].

However, relatively little work has been presented on the temporal and spatial characterisation of the evolution of the fatigue damage evolution in aluminum alloys with localized corrosion, specifically, in the form of quantitative, full-field, full-process experimental observations. Recently, the authors employed the digital image correlation (DIC) technique, to measure the material surface deformation field thus providing full-field, real-time, non-contact measurement [21-23]. This facilitated detailed interrogation of the failure evolution process for pre-corroded aluminum alloy [24]. However, there is a need for quantitative and qualitative analysis of the fatigue damage evolution process, especially with respect to loading conditions and local corrosion morphology. To this end, the current paper presents a combined methodology using DIC analysis and SEM-based analysis of fracture morphology for fatigue damage in pre-corroded aluminum, considering different loading conditions and corrosion diversity. Constant amplitude fatigue tests with three different levels of maximum stress were conducted on pre-corroded AA7075-T7651 specimens. For each loading conditions, three pre-corroded specimens with the same corrosion exposure time were tested. The analysis combines measured damage curve, strain field evolution and fracture morphology investigation.

2. Experiment

2.1. Material and specimen

The material studied in this paper is AA7075-T7651 (Si-0.4 Ti-0.2 Cr-0.18-0.28 Fe-0.5 Mg-2.1-2.9 Cu-1.2-2.0 Mn-0.3 Zn-5.1-6.1 Al; wt%). The elastic modulus, yield strength and tensile strength of the material are 84.6 GPa, 486.8 MPa and 520.2 MPa respectively. The specimen preparation procedure consists of: mechanical machining, pre-corrosion and painting. First, the material was cut into dog-bone shaped specimens for fatigue tests refer to ASTM E 466-15, as shown in Fig. 1(a). The metallographic structure of the L-T plane of AA7075-T7651 is shown in Fig. 1(b). Secondly, to produce prior corrosion damage, specimens were immersed in standard exfoliation corrosion (EXCO) solution (234g/L NaCl, 50g/L KNO_3 and 6.3mL/L HNO_3) for 48 hours according to ASTM G34-01 [25]. Then all the pre-corroded specimens were rinsed and ultrasonically cleaned in ethyl alcohol. Fig. 1 (c) shows the weight loss-time curve for the corrosion of AA7075-T7651 in EXCO solution, which varies almost linearly with time. The mass loss for corrosion 48 hours is 64.4 g/m^2. Finally, to facilitate DIC analysis in fatigue tests, random black and white speckles were created on all the fatigue specimens'

surfaces by spraying paints.

2.2. Experimental procedure

Constant amplitude uniaxial fatigue tests with different levels of maximum stresses were successively performed on both un-corroded and pre-corroded specimens using an Instron 8803 fatigue testing machine at room temperature. The applied axial load was controlled to apply sine wave load in all tests, as shown in Fig. 2 (a). Three different maximum stresses of 278 MPa, 333 MPa, 389 MPa were applied respectively. The stress ratio (R) is set as 0.1 for all tests and the loading frequency is 5 Hz. Three test replicates were done for each loading condition.

During the loading process, stereo images of the specimen surface in specified fatigue cycles were captured by the commercial software VIC-3D (Correlated Solutions, Inc.). Since the quality of captured speckle image in active status is lower than that in the static condition, the load was temporarily interrupted to maintain peak value when taking the images, as shown in Fig. 2 (b). The resolution of the CCD capture region was 1524×3205 pixels. After fatigue testing, the acquired stereo image sequences of specimens were processed by VIC-3D software to obtain the displacement and strain fields on the specimen surfaces. Here a subset size of 27 × 27 pixels was chosen, with a step length of 2 pixels. Strain fields were calculated to visually display the temporal and spatial characteristics of macro-crack initiation and propagation up to failure, while damage severity curves were simultaneously derived, based on the statistical analysis of strain fields to describe damage evolution of the whole specimen. Finally, the fracture surfaces of the key macro-crack initiation regions, as identified by DIC, were further interrogated by SEM, to characterize the micro-cracking phenomena.

3. Results

3.1. Fatigue lives under different peak loads

The measured fatigue lives of un-corroded and pre-corroded specimens under different loading conditions are shown in Fig. 3. The average lives of pre-corroded specimens are 46,580, 23,502, 13,478 cycles corresponding to applied maximum stresses of 278 MPa, 333 MPa, 389 MPa, respectively, while the average lives of the un-corroded specimens are 71,598, 32,038, 20,744 cycles; hence, the lives decreased by 34.9%, 26.6%, and 35.1%, respectively. The experimental results indicate that pre-corrosion severely degrades the fatigue behaviour of AA7075-T7651; this is attributed to stress concentrations due to localized corrosion causing accelerated crack initiation and hence reducing fatigue life. The measured fatigue lives of three pre-corroded specimens with a maximum stress of 389 MPa were 11,520, 12,030, and 16,884 respectively, showing relatively high scatter for this high stress level, due to the stochastic variation of localized corrosion. In contrast, negligible scatter in life was observed for the low stress levels. Hence, high maximum stress amplifies the effect of localized corrosion on fatigue life, by providing a high driving force (effective stress intensity factor range) for crack propagation.

3.2. Fatigue damage evolution by DIC

Corresponding to the degradation of fatigue life, the DIC method is used to describe the damage evolution in the test specimens throughout the entire fatigue process, consisting of a fatigue damage curve and strain field

evolution. It is well known that DIC can provide full-field maps of strain on the specimen surface to visualize damage evolution, including localization of strain, crack initiation and propagation. Based on statistical analysis of these measured strain fields, various metrics for damage assessment can be derived to characterize the corresponding evolution of full-field damage. For example, a damage severity factor, reflecting the deviation from the average deformation, has been proposed to characterize damage severity degree of the material [26].

3.2.1. Fatigue damage severity curve

Herein, we apply the so-called damage severity factor to describe damage evolution under fatigue loading. More detailed description of the factor can be found in the literature [26]. Based on the DIC-measured strain fields, it is possible to plot specific measures of strain for the specimen as a function of number of fatigue cycles, including (i) the average strain value over all points, and (ii) the strain values at selected 'hot-spot' points with high strain values. For example, Fig. 4 (a) shows the average strain over all points as a function of cycles, as well as the strain versus cycles response as selected points corresponding to the highest 1% and 10% of strain, in a typical pre-corroded specimen. The overall average strain is almost unchanged before the failure point, which obscures identification of key stages in the damage evolution process; however, the average of selected points increased slowly in the initial stage, followed by an inflection point, and then finally increases rapidly. Compared to other points, the values in the selected group of points with highest strain levels increase more gradually. To describe the change in value, the following parameter is defined:

$$\bar{\varepsilon} = \left(\frac{1}{m} \sum_{i=1}^{m} (\varepsilon_1)_i - \frac{1}{N} \sum_{i=1}^{N} (\varepsilon_1)_i \right) \tag{1}$$

where $(\varepsilon_1)_i$ is the magnitude of the maximum tensile strain ε_1 at point i, m is the number of selected points with highest strain (above a given % level), and N is the overall number of points. Specifically, $\bar{\varepsilon}$ quantifies the deviation of selected points from the global average deformation, which can be used to describe the damage severity. $\bar{\varepsilon}$ increases with damage accumulation, and reaches a maximum at failure. Hereafter, we normalize $\bar{\varepsilon}$ by the value at the failure point, to represent damage severity degree as:

$$D_f = \bar{\varepsilon} / \bar{\varepsilon}_{\max} \tag{2}$$

D_f is referred to as damage severity factor. D_f increases gradually with fatigue cycles and finally reaches about 1 at failure.

Herein, we have taken selected points with the highest 1% of strain to calculate D_f due to the relatively high sensitivity, as shown in Fig. 4 (a). Fig. 4 (b) shows the damage severity curves of un-corroded and pre-corroded specimens during fatigue loading. It can be seen that the failure process consists of three stages. At first, D_f increases slowly consuming the majority of the fatigue life, termed hereafter as the 'damage accumulation' stage. In the second stage, D_f increasing at an increasing rate, leading to an inflection point, identified as 'macro-crack initiation'. Finally, D_f increases very rapidly, corresponding to the 'macro-crack propagation' stage. The experimental results clearly show that pre-corrosion significantly accelerates the fatigue damage accumulation, promoted crack initiation, and hence reducing life.

3.2.2. Strain field evolution

Combined with the damage severity curve, the strain fields on the specimen surfaces at specified numbers of cycles were obtained to visualize the temporal and spatial characteristics of fatigue damage evolution including damage accumulation, macro-crack initiation and macro-crack propagation, particularly with respect to effect of loading conditions. It should be noted that, considering that the field of view for our DIC tests is at a macro scale (macro-DIC), the stage of crack initiation identified by DIC refers to the macro-crack initiation, and the micro-crack initiation and development related to some microscopic roughness and crack belong to the damage accumulation stage. Fig. 5 shows the maximum tensile strain fields of three repeated specimens with maximum stress of 278 MPa, along with the computed damage severity curves. For specimen 1-1, no evident damage localization was detected before 3.5×10^4 cycles (A_1 in Fig. 5). After 4.26×10^4 cycles, corresponding to reflection point B_1 in the damage severity curve, a strain localization region I_1 appeared at the left edge and near the mid-length of specimen (B_1 in Fig. 5, indicated by the white arrow), reflecting formation of macro-crack I_1 due to gradual damage localization. Macro-crack I_1 gradually propagated with increasing cycles (C_1 in Fig. 5), while another strain concentration region I_2 appeared simultaneously at 4.94×10^4 cycles. However, the appearance of region I_2 did not change the cracking path of crack I_1, and the propagation of macro-crack I_1 led to final failure (D_1 in Fig. 5). For specimen 1-2, the distribution of strain field seems to be uniform before 3.5×10^4 cycles (A_2 in Fig. 5). At 4.0×10^4 cycles, a strain concentration region II_1 appeared at the left edge and near the mid-length of specimen (B_2 in Fig. 5, indicated by the white arrow), leading to macro-crack initiation, corresponding to inflection point B_2. With increasing cycles, macro-crack II_1 continued propagating (C_2 in Fig. 5), leading to final failure (D_2 in Fig. 5). For specimen 1-3, after damage accumulation, two strain localized regions III_1 and III_2 were found on both sides and away from the mid-length of the specimen at 4.15×10^4 cycles (B_3 in Fig. 5), indicating that two macro-cracks had nucleated in these two regions, corresponding to inflection point B_3 in the damage severity curve. After 4.74×10^4 cycles, multiple macro-cracks appeared on the edges and surface of specimen, e.g. macro-cracks III_1, III_2, III_3 and III_4 (C_3 in Fig. 5). Finally, the propagation of main macro-cracks III_1 and III_3 led to failure at 47,493 cycles. Macro-crack III_2 did not grow further although it appeared earlier than macro-crack III_3, and macro-crack III_4 affected the cracking path of III_1 (D_3 in Fig. 5).

Fig. 6 shows the evolution of maximum tensile strain field in the three repeat specimens with maximum stress 333 MPa. For specimen 2-1, strain localization was not obvious until 1.2×10^4 cycles (A_4 in Fig. 6). After that, two regions with high strain appeared at 1.75×10^4 cycles: region IV_1 located at the right edge and away from the mid-length of specimen, and region IV_2 located at the specimen surface near region IV_1 (B_4 in Fig. 6, indicated by the arrow). These indicate macro-crack initiation in these two regions, corresponding to the inflection point B_4 in the damage severity curve. Macro-crack IV_2 grew quickly with fatigue loading from 1.75×10^4 cycles to 2.15×10^4 cycles (C_4 in Fig. 6), and led to final failure at 22,242 cycles (D_4 in Fig. 6). For specimen 2-2, there was also no evident localized damage until 1.2×10^4 cycles (A_5 in Fig. 6). Then, after 1.75×10^4 cycles, a strain concentration region V_1, appeared at the left edge and away from the mid-length of specimen, (B_5 in Fig. 6, indicated by the arrow) where the strain value is obviously higher than in other regions. This indicates crack initiation corresponding to the inflection point B_5 in the damage severity curve. Macro-crack V_1 was observed to propagate gradually with increasing fatigue cycles (C_5 in Fig. 6), leading to final failure at 22,242 cycles (D_5 in Fig. 6). For specimen 2-3, no strain localization region was detected until 1.75×10^4 cycles (A_6 in Fig. 6). After 2.3×10^4 cycles, a macro-crack VI_1 appeared on the right side and away from the

mid-length of the specimen (B_6 in Fig 6), corresponding to the inflection point B_6. Another macro-crack VI_2 formed on the left edge and near the mid-length of specimen at 2.72×10^4 cycles (C_6 in Fig. 6). Macro-cracks VI_1 and VI_2 simultaneously propagated and led to the fracture at 27,401 cycles (D_6 in Fig. 6).

For the maximum stress of 389 MPa, damage evolution can be deduced from the DIC strain maps shown in Fig. 7. For specimen 3-1, after damage accumulation and localization, macro-crack VII_1 nucleated at the left side and near the mid-length of specimen at 9×10^3 cycles (B_7 in Fig. 7, indicated by the white arrow), corresponding to the inflection point B_7 in the damage severity curve. Macro-crack VII_1 gradually enlarged and propagated with increasing cycles (C_7 in Fig. 7), while another crack VII_2 was observed to develop on the surface at 1.14×10^4 cycles. Finally, the propagation of main macro-crack VII_1 caused failure at 11,520 cycles (D_7 in Fig. 7). For specimen 3-2, there was no evident localized damage before 8×10^3 cycles (A_8 in Fig. 7). Then two regions $VIII_1$ and $VIII_2$ with high local strain appeared at the edge and near the mid-length of specimen (B_8 in Fig. 7, indicated by the arrow) at 8.6×10^3 cycles, corresponding to inflection point B_8 in the damage severity curve. Main macro-cracks $VIII_1$ grew quickly with increasing cycles (C_8 in Fig. 7), leading to final failure at 12,030 cycles (D_8 in Fig. 7). For specimen 3-3, apparent damage localization was not observed at 1.2×10^4 cycles; then a strain localization region IX_1 was found at the right edge and near the mid-length of the specimen at 1.55×10^4 cycles (B_9 in Fig. 7, indicated by the arrow), indicating macro-crack initiation, corresponding to inflection point B_9. Macro-crack IX_1 gradually propagated with increasing cycles (C_9 in Fig. 7), leading to final failure at 16,884 cycles (D_9 in Fig. 7).

3.3. Fracture morphology analysis

The DIC results presented above show that the initiation and propagation of primary macro-cracks dominated the failure process. Post-failure fracture morphology analysis for specimens under different loading conditions was carried out, mainly focusing on the main macro-crack initiation regions, for more detailed interrogation of the interaction between localized corrosion and fatigue failure. Fig. 8 shows the fracture morphology of three specimens with maximum stress 278 MPa, corresponding to the main macro-crack initiation regions identified by the DIC strain fields shown in Fig. 5. A main micro-crack site and a second micro-crack site were observed on the L-S surface of specimen 1-1, as shown in Fig. 8 (a), corresponding to macro-crack II_1 initiation region. The propagation and coalescence of these two micro-cracks formed a ridge. An enlarged view of the main micro-crack initiation site was further given in Fig. 8 (b), which demonstrated that the micro-crack originated from a wide, shallow localized corrosion feature. The formation of localized corrosion in high strength aluminum alloy is normally associated with some fraction of constituent particles, such as Al_7Cu_2Fe, Al_3Fe, and Al_6Mn. The significant difference in electrochemical behavior from the surrounding matrix phase causes such particles to act as cathodic sites to the matrix of aluminum (anodic), leading to localized corrosion in some areas of the sample [27, 28]. Fig. 8 (c) shows the fracture morphology of the macro-crack II_1 initiation region in specimen 1-2, corresponding to the strain fields shown in Fig. 5. A micro-crack initiation site was observed on the L-T surface. From the enlarged view shown in Fig. 8 (d), the micro-crack developed from an approximate semi-elliptical localized corrosion. Quasi-cleavage fracture features are observed in the fracture morphology, indicating that the pre-corrosion causes material embrittlement. The macro-crack III_1 initiation region of

specimen 1-3 is shown in Fig. 8 (e); it was also observed that a micro-crack initiated at the L-T surface. The enlarged view shows that the micro-crack initiated from an irregular wide, shallow localized corrosion feature.

Fig. 9 shows the fracture morphology of three specimens with maximum stress 333 MPa, corresponding to the strain maps shown in Fig. 6. For specimen 2-1, a micro-crack initiation site was identified at the L-S surface, with localized corrosion and obvious quasi-cleavage fracture features, as shown in Fig. 9 (a) and (b). The fracture morphology of macro-crack V_1 (specimen 2-2) is shown in Fig. 9 (c). A micro-crack initiation site was found at the L-S surface. Fig. 9 (d) shows an enlarged view, indicating a wide shallow localized corrosion feature as the origin. For specimen 2-3, main and secondary micro-cracks were identified at the L-T surface from the macro-crack VI_2 initiation region, as shown in Fig. 9 (e). The main micro-crack also initiated from localized corrosion, as shown in Fig. 9 (f).

Fig. 10 shows the fracture morphology from the three specimens with maximum stress 389 MPa, corresponding to strain fields in Fig. 7. Fig. 10 (a) shows the fracture morphology of macro-crack VII_1. A main micro-crack at the corner and a secondary micro-crack at the L-S surface was observed. Fig. 10 (b) shows that the main micro-crack originated from a wide shallow localized corrosion defect. Similarly, for specimen 3-2, a corner micro-crack at the edge of L-S surface and a surface micro-crack at L-S plane were observed in the main macro-crack initiation region $VIII_1$, as shown in Fig. 10 (c). The enlarged view of the main micro-crack, shown in Fig. 10 (d), demonstrated that micro-crack nucleation was caused by localized corrosion. As shown in Fig. 10 (e), macro-crack initiation region IX_1 in specimen 3-3 contains a main micro-crack and a secondary micro-crack located on the L-T surface. Fig. 10 (f) also indicates that the main micro-crack originated from a narrow and deep localized corrosion region.

4. Discussion

The phenomena that fatigue cracks originate from localized corrosion, accompanied with typical quasi-cleavage fracture characteristics, is consistent with previous work reported [14, 29-31], which reveals that stress concentration at localized corrosion accelerates crack initiation. In the present work, the methodology using a combination of damage severity curves, DIC-measured strain maps, and detailed SEM fracture morphology, provides a quantitative and qualitative characterisation of the entire corrosion-nucleated fatigue failure process, under a range of loading conditions.

The experimental results showed that localized corrosion penetrated the specimen surfaces significantly and hence significantly affected the location of fatigue crack initiation. Some macro-crack initiation regions were located away from the mid-length of the specimen, such as macro-cracks III_3 and IX_1, shown in Fig. 5 and Fig. 7, respectively, with relatively low stress compared to the mid-length. This phenomena demonstrates that corrosion damage can significantly affect location of fatigue crack nucleation. Multiple corrosion-induced cracks were observed to initiate and evolve under different loading conditions, and most main macro-cracks nucleated in the L-S surface. The damage evolution and failure processes different temporally and spatially between specimens with the same loading conditions, due to the stochastic variation in localized corrosion, presumably due to metallurgical, microstructural and topographical variations. Experimental results also showed that high maximum stress promoted macro-crack initiation, hence leading to the fatigue life reduction. At the highest maximum stress, multiple micro-crack initiations were observed in all specimens, as shown in the fracture

morphology of Fig. 10, which is consistent with previously-published observations that multiple cracks are readily nucleated under high maximum stress [7]. Three typical failure modes (single crack fracture, multi-crack competition and multi-crack parallel growth) were observed. For the single macro-crack mode, such as specimen 1-1 and 1-2, shown in Fig.5, the single crack originated from localized corrosion and propagated with increasing cycles up to fracture. In addition, multiple macro-cracks were found to initiate in different regions at the specimen surface, which can be distinguished as multi-crack competition and multi-crack parallel growth. For the multi-crack competition mode, two or more cracks initiated in some adjacent regions, but only one of these eventually formed the main crack and led to failure, e.g. specimen 3-2 in Fig. 7. For the multi-crack parallel growth mode, multiple cracks were found to grow in parallel, simultaneously, e.g. specimen 2-3 in Fig. 6. The experimental results showed that the fracture paths were quite different in the different modes. These fracture modes were determined by the coupled effect of loading condition and relative location of macro-crack initiation regions, related to the spatial distribution of localized corrosion.

5. Conclusions

The damage evolution of aluminum alloy 7075-T7651 under different levels of maximum stress in constant amplitude fatigue tests was experimentally investigated using a combined analysis consisting of damage severity curves, DIC-based strain mapping and SEM-based fracture morphology. It is concluded that:

(1) The damage severity factor was presented based on statistical analysis of the DIC-based strain fields, to characterise the fatigue damage evolution, including damage accumulation, macro-crack initiation and propagation. It was shown that prior corrosion of 48 hours in EXCO solution led to accelerated macro-crack initiation for all loading conditions investigated, with an associated reduction in fatigue life of between about 27% and 35%.

(2) DIC results showed that the damage evolution and failure process differed temporally and spatially, even in specimens with the same loading conditions, due to stochastic variation of localized corrosion. Penetration of localized corrosion in the ‘L-S’ or ‘L-T’ surfaces promotes fatigue crack initiation, affecting crack nucleation location, cracking path, and is accompanied with quasi-brittle fracture.

(3) Multiple corrosion-induced cracks were observed to initiate and evolve under different loading conditions: Three typical failure modes were observed, namely, single crack fracture, multi-crack competition and multi-crack parallel growth, depending on loading condition and relative location of macro-crack initiation.

Data Availability Statement

The raw/processed data required to reproduce these findings cannot be shared at this time as the data also forms part of an ongoing study.

Acknowledgements

This research was supported by the National Natural Science Foundation of China (NSFC, Grant Nos. 11972364, 11502285 and 51971242), the Foundation of Jiangsu Province Key Laboratory of Aerospace Power System, the Scientific Research Foundation of Civil Aviation University of China (SRFCAUC, Grant No. 2013QD23X) and the Science Foundation Ireland (SFI, Grant No. 14/IA/2604).

References

[1] T. Dursun, C. Soutis, Materials & Design (1980-2015), 56 (2014) 862-871.
[2] K.K. Sankaran, R. Perez, K.V. Jata, Materials Science and Engineering: A, 297 (2001) 223-229.
[3] N.D. Alexopoulos, P. Papanikos, Materials Science and Engineering: A, 498 (2008) 248-257.
[4] L. Molent, Engineering Fracture Mechanics, 137 (2015) 12-25.
[5] J.J. Medved, M. Breton, P.E. Irving, International Journal of Fatigue, 26 (2004) 71-80.
[6] K. Genel, Scripta Materialia, 57 (2007) 297-300.
[7] K. van der Walde, J.R. Brockenbrough, B.A. Craig, B.M. Hillberry, International Journal of Fatigue, 27 (2005) 1509-1518.
[8] S. Kim, J.T. Burns, R.P. Gangloff, Engineering Fracture Mechanics, 76 (2009) 651-667.
[9] K. van der Walde, B.M. Hillberry, International Journal of Fatigue, 29 (2007) 1269-1281.
[10] A.T. Kermanidis, P.V. Petroyiannis, S.G. Pantelakis, Theoretical and Applied Fracture Mechanics, 43 (2005) 121-132.
[11] N.E.C. Co, J.T. Burns, International Journal of Fatigue, 103 (2017) 234-247.
[12] X.-D. Li, X.-S. Wang, H.-H. Ren, Y.-L. Chen, Z.-T. Mu, Corrosion Science, 55 (2012) 26-33.
[13] G. Joshi, S. Mall, Journal of Materials Engineering and Performance, 26 (2017) 2293-2304.
[14] J.T. Burns, J.M. Larsen, R.P. Gangloff, Fatigue & Fracture of Engineering Materials & Structures, 34 (2011) 745-773.
[15] J. LIU, B. CHEN, X. YE, B. HU, C. DING, X. WU.
[16] M. Amiri, A. Arcari, L. Airoldi, M. Naderi, N. Iyyer, Corrosion Science, 98 (2015) 678-687.
[17] P. Hu, Q.C. Meng, W.P. Hu, F. Shen, Z.X. Zhan, L.L. Sun, Corrosion Science, 113 (2016) 78-90.
[18] M. McMurtrey, D. Bae, J. Burns, Fatigue & Fracture of Engineering Materials & Structures, 40 (2017) 605-622.
[19] Y. Xiang, Y. Liu, Engineering Fracture Mechanics, 77 (2010) 1314-1324.
[20] C.Q. Wang, J.J. Xiong, R.A. Shenoi, M.D. Liu, J.Z. Liu, International Journal of Fatigue, 83 (2016) 280-287.
[21] B. Pan, K. Qian, H. Xie, A. Asundi, Measurement Science and Technology, 20 (2009) 062001.
[22] X. Zhang, Y. Wang, J. Yang, Z. Qiao, C. Ren, C. Chen, Optics and Lasers in Engineering, 85 (2016) 24-28.
[23] Z.L. Ning, W.Z. Liang, Z.J. Kang, H.C. Sun, J.F. Sun, Materials Science and Engineering a-Structural Materials Properties Microstructure and Processing, 697 (2017) 233-237.
[24] H. Song, Z. Bai, H. Zhang, Y. Niu, S. Leen, Fatigue & Fracture of Engineering Materials & Structures, (2018).
[25] A. Standard, Standard Test Method for Exfoliation Corrosion Susceptibility in 2XXX and 7XXX Series Al Alloys, (2001).
[26] H. Song, H. Zhang, D. Fu, Q. Zhang, International Journal of Rock Mechanics and Mining Sciences, 88 (2016) 157-164.
[27] N. Birbilis, M.K. Cavanaugh, R.G. Buchheit, Corrosion Science, 48 (2006) 4202-4215.
[28] F. Andreatta, M. Lohrengel, H. Terryn, J. De Wit, Electrochimica Acta, 48 (2003) 3239-3247.
[29] Y.F. Huang, X.B. Ye, B.R. Hu, L.J. Chen, International Journal of Fatigue, 88 (2016) 217-226.
[30] M. Weber, P.D. Eason, H. Ozdes, M. Tiryakioglu, Materials Science and Engineering a-Structural Materials Properties Microstructure and Processing, 690 (2017) 427-432.
[31] C.A. Arriscorreta, D.W. Hoeppner, Corrosion, 68 (2012) 950-960.

Figure Captions

Fig. 1. (a) Schematic diagram of specimen for fatigue tests, (b) microstructure of AA7075-T7651 along the L-S direction, (c) weight loss-time curve for the corrosion of AA7075-T7651in EXCO solution.

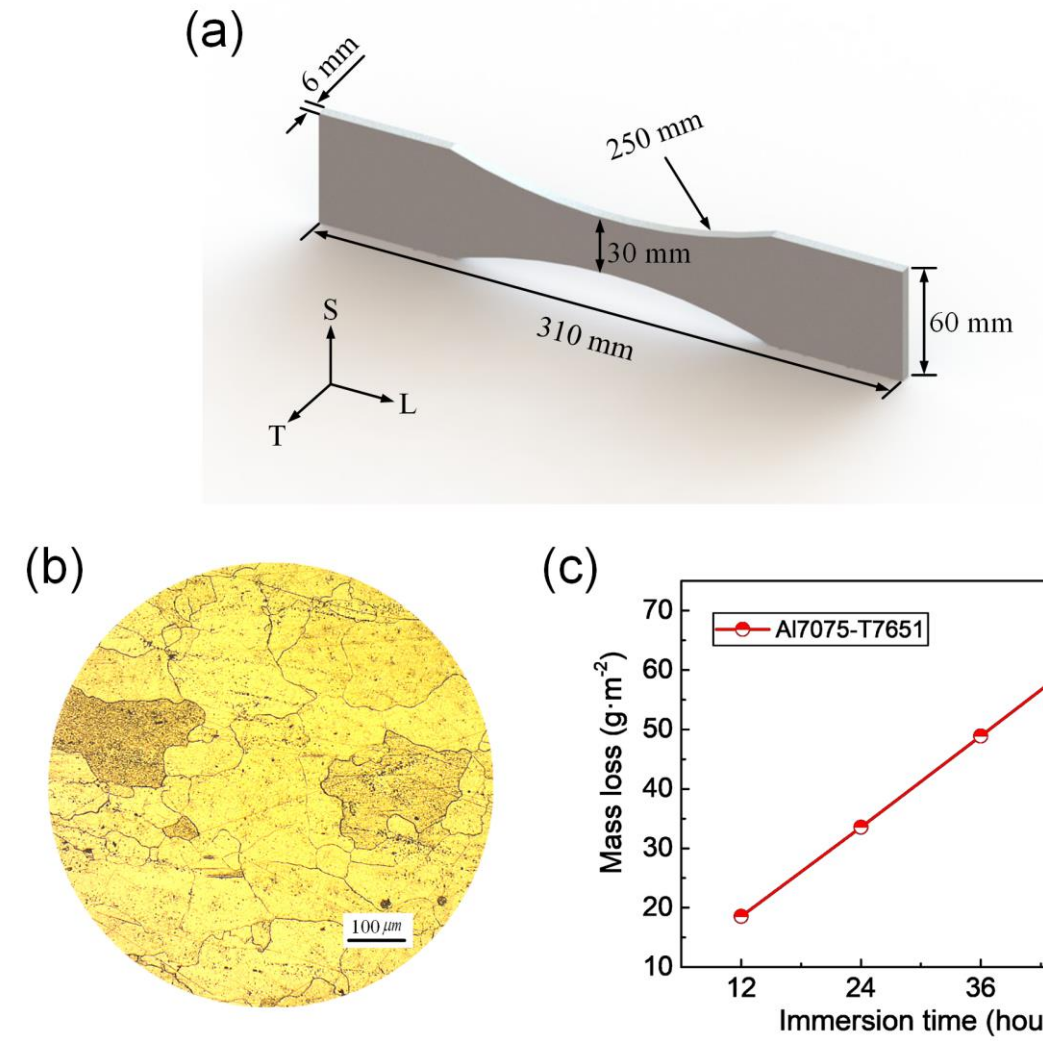

Fig. 1. (a) Schematic diagram of specimen for fatigue tests, (b) microstructure of AA7075-T7651 along the L-S direction, (c) weight loss-time curve for the corrosion of AA7075-T7651in EXCO solution.

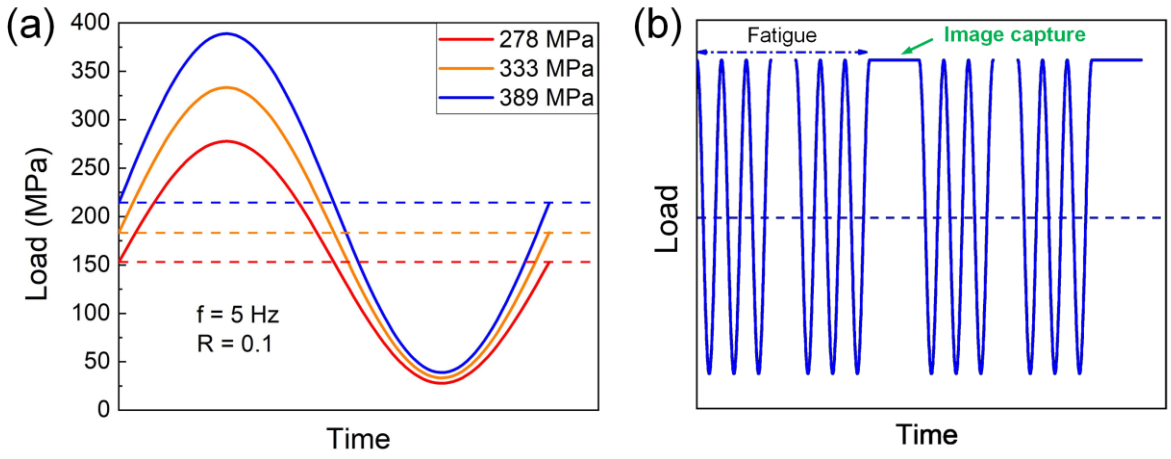

Fig. 2. (a) Applied fatigue stress waveforms, (b) schematic diagram of load spectrum.

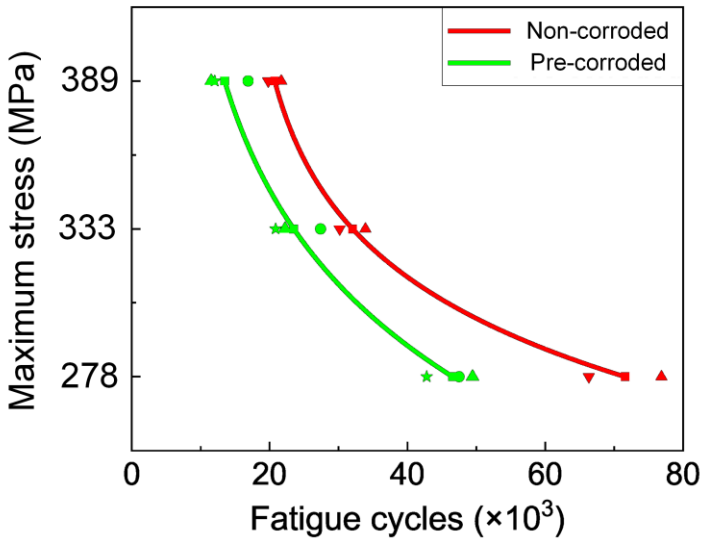

Fig. 3. Measured fatigue life of un-corroded and pre-corroded AA7075-T7651 under different peak load.

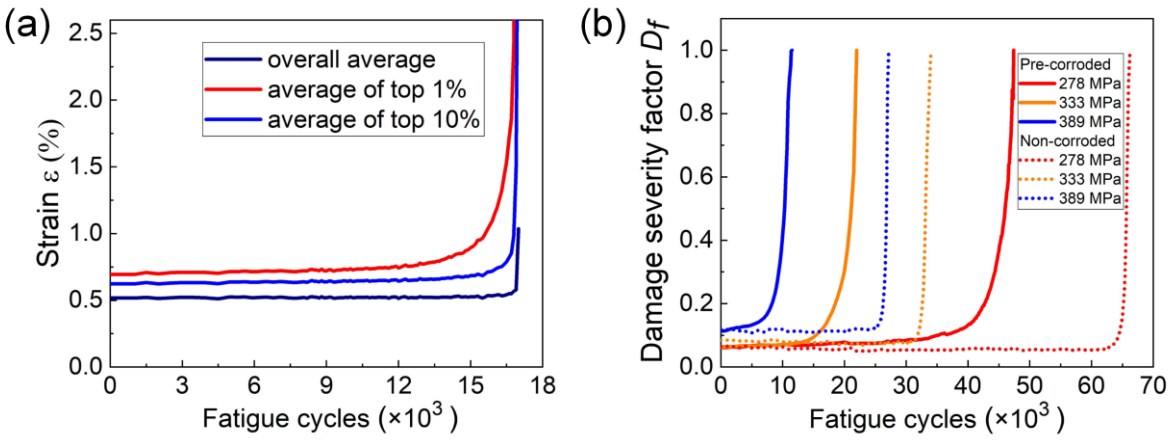

Fig. 4. (a) The average values of all points, the top 1% and 10% of maximum tensile strain points versus fatigue cycle, (b) damage severity curves of un-corroded and pre-corroded AA7075-T7651 specimens.

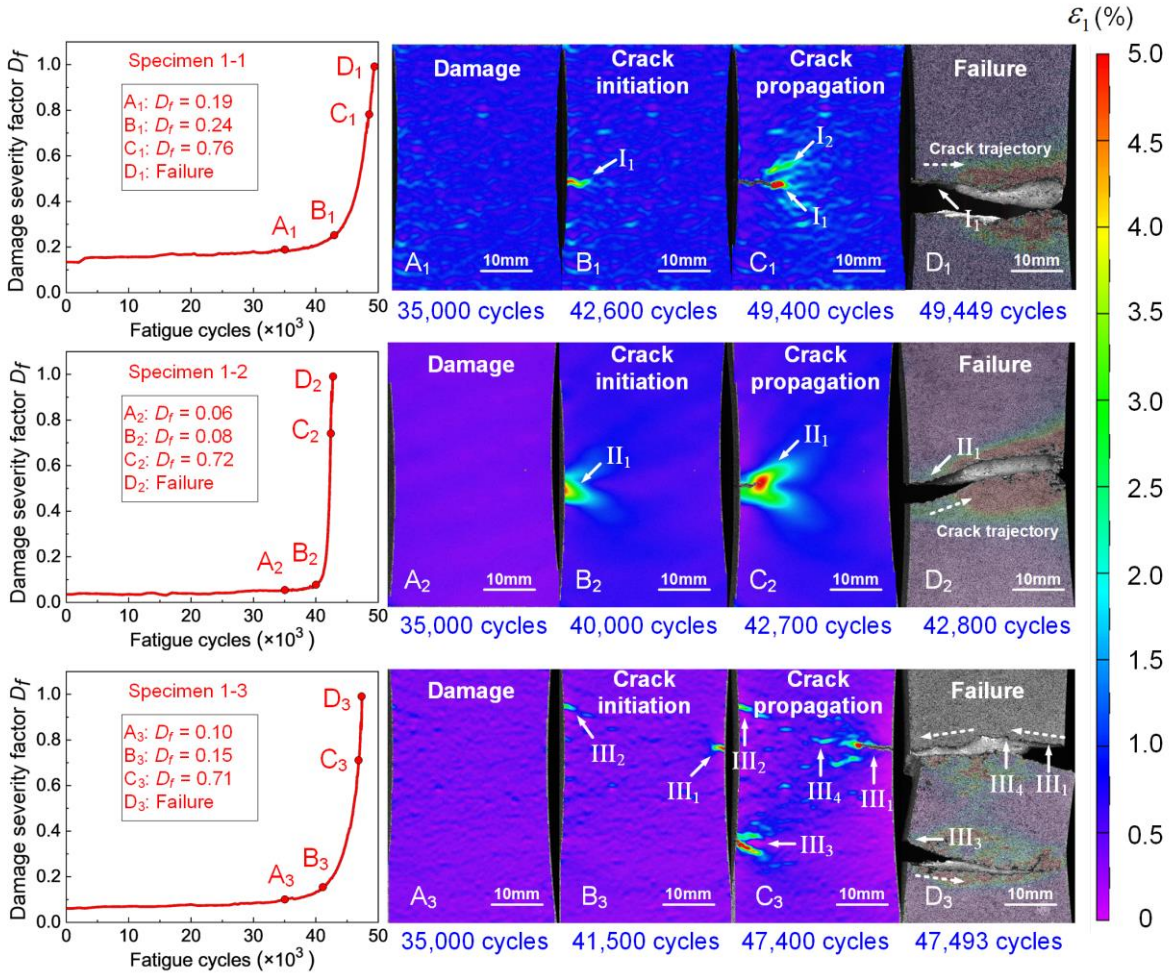

Fig. 5. Visualization of damage evolution, crack initiation and propagation in pre-corroded AA7075-T7651 specimens with a maximum stress of 278 MPa, represented by damage severity curves and maximum tensile strain fields shown in the colored images.

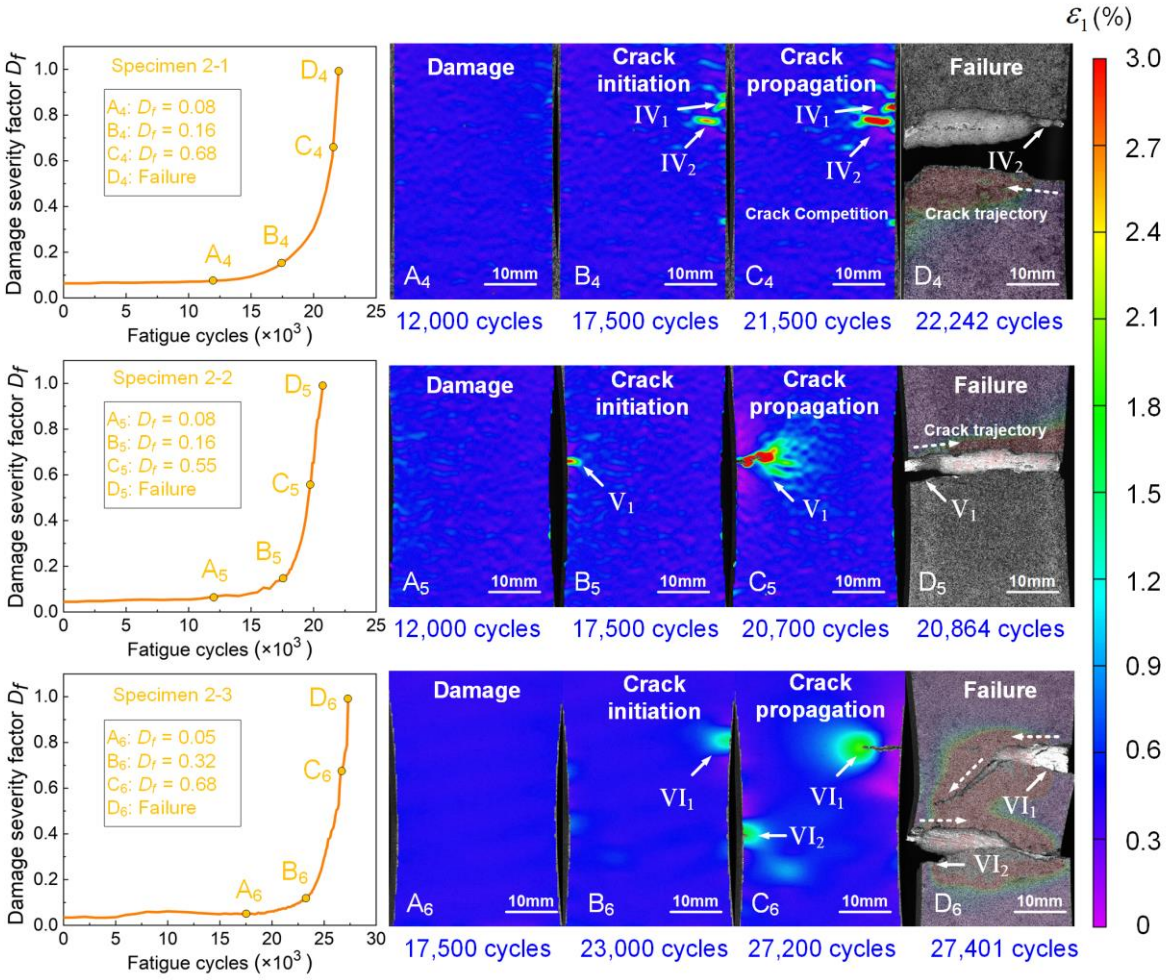

Fig. 6. Visualization of damage evolution, crack initiation and propagation in pre-corroded AA7075-T7651 specimens with a maximum stress of 333 MPa, represented by damage severity curves and maximum tensile strain fields shown in the colored images.

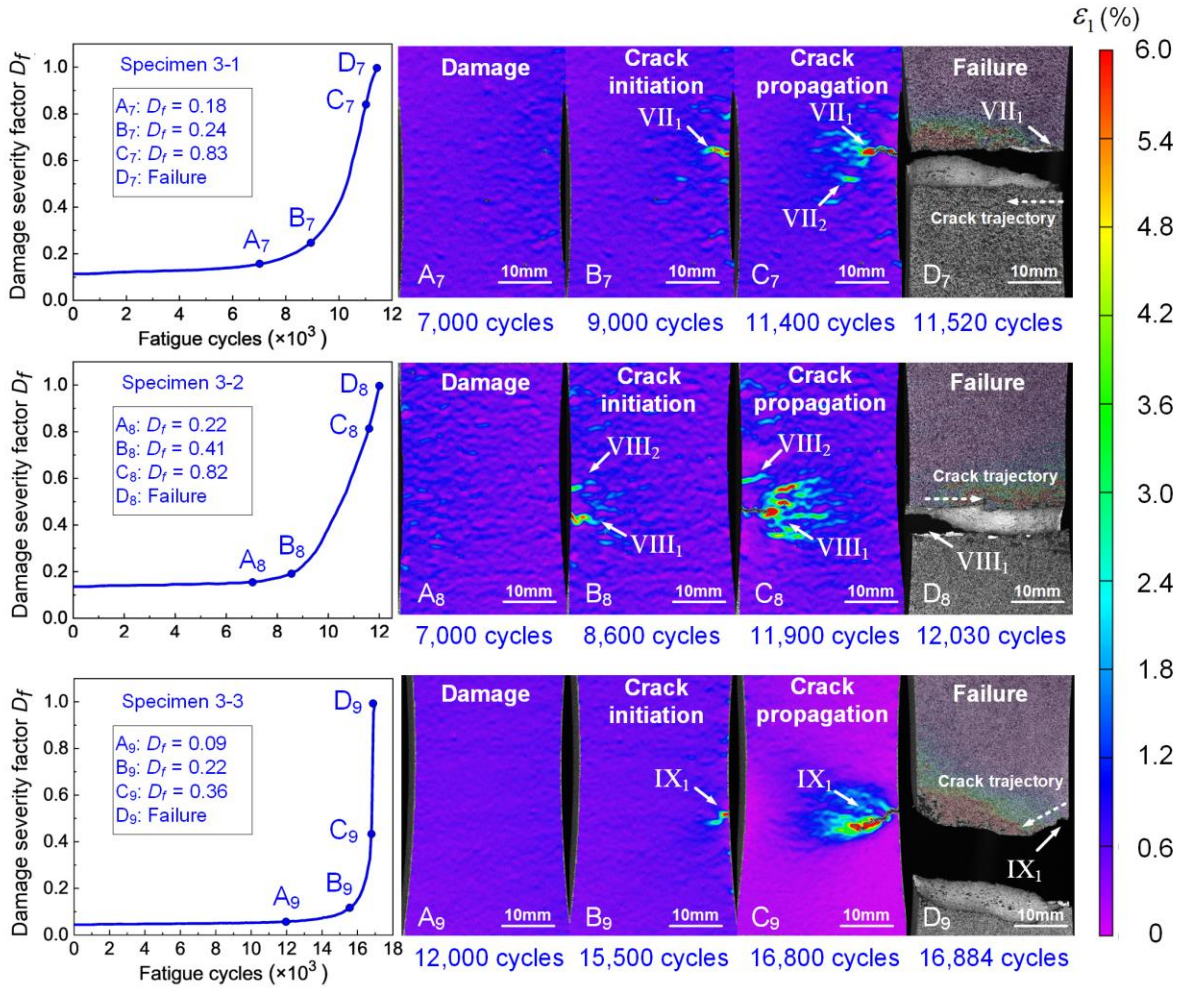

Fig. 7. Visualization of damage evolution, crack initiation and propagation in pre-corroded AA7075-T7651 specimens with a maximum stress of 389 MPa, represented by damage severity curves and maximum tensile strain fields shown in the colored images.

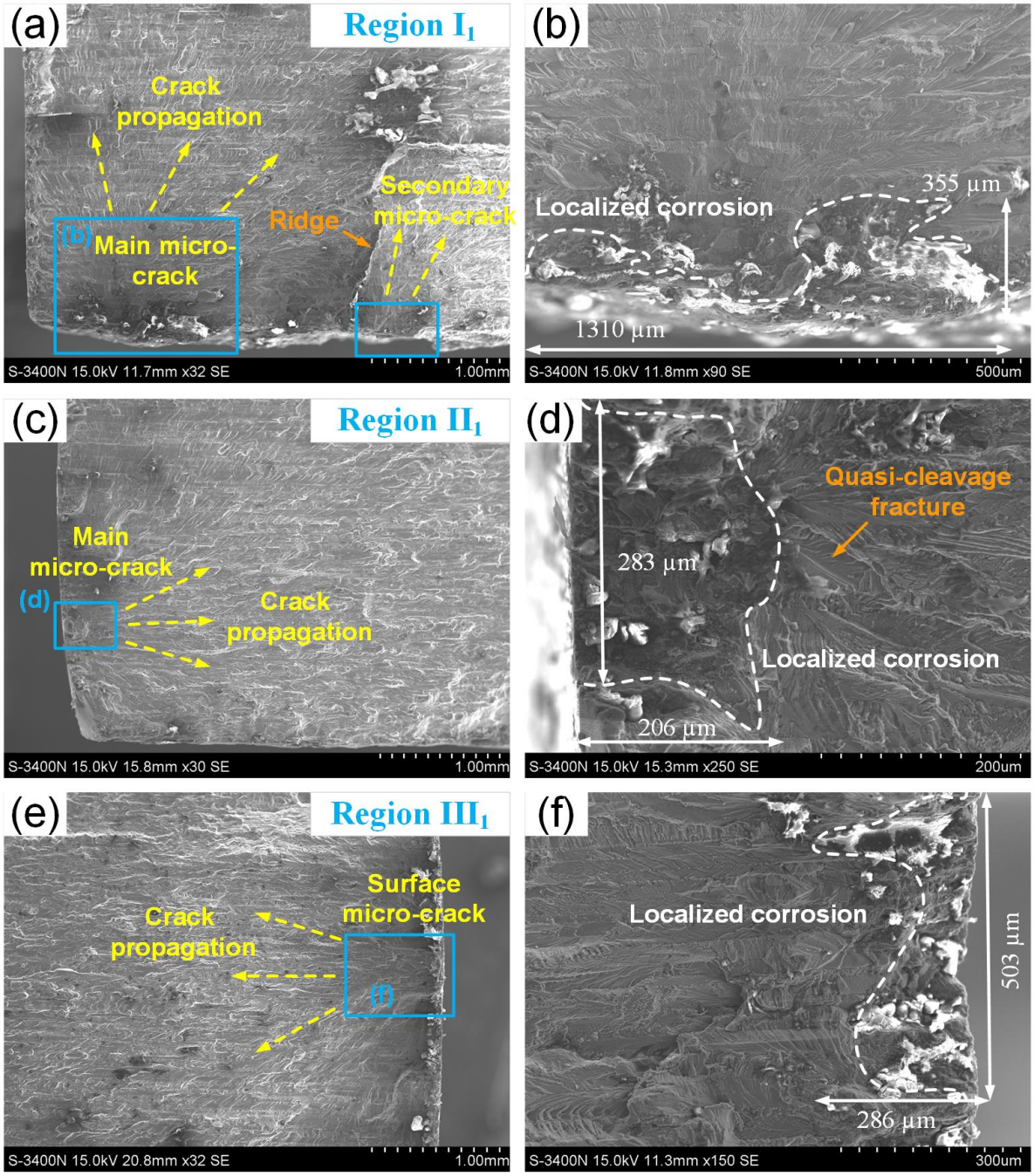

Fig. 8. Typical fracture morphology of pre-corroded AA7075-T7651 specimens with a maximum stress of 278 MPa.

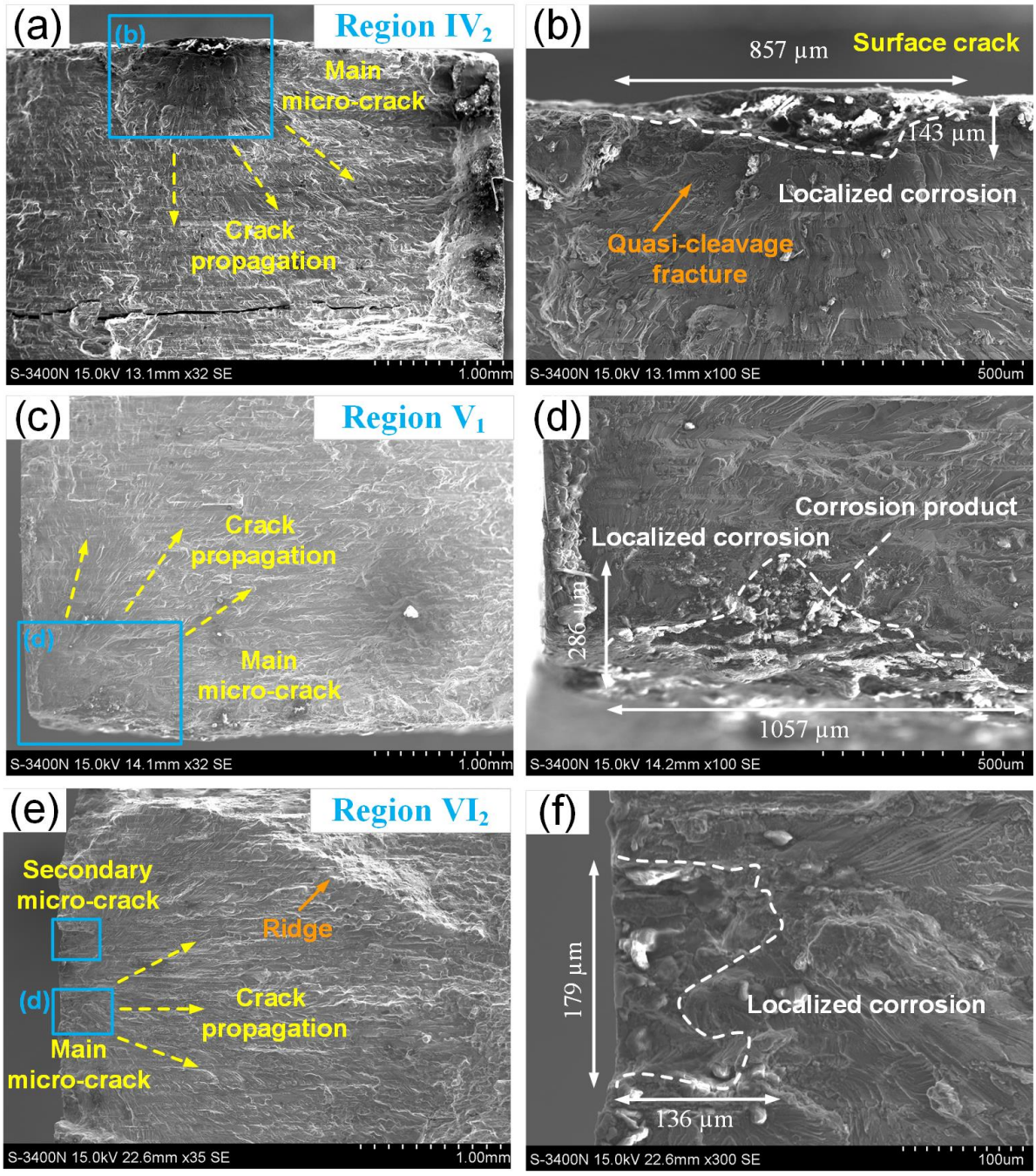

Fig. 9. Typical fracture morphology of pre-corroded AA7075-T7651 specimens with a maximum stress of 333 MPa.

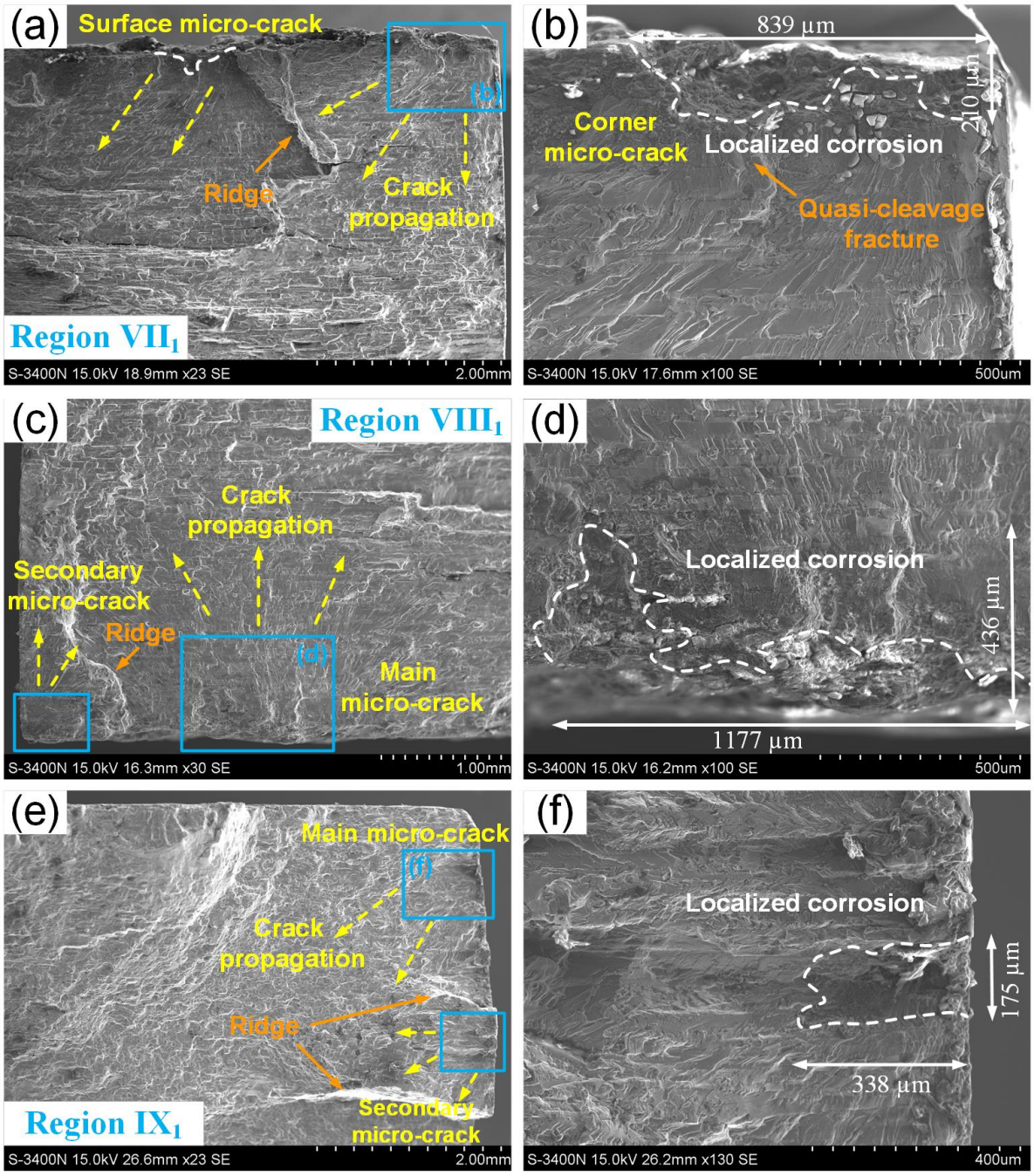

Fig. 10. Typical fracture morphology of pre-corroded AA7075-T7651 specimens with a maximum stress of 389 MPa.